

Corresponding Author:

Daniel P. Babin: ORCID: 0000-0002-8339-1312

Lamont Doherty Earth Observatory
Geochemistry Division
Columbia University
Department of Earth and Environmental Science

Co-Authors:

Allison M. Franzese

Lamont Doherty Earth Observatory
Geochemistry Division
Hostos Community College
Physical Sciences Unit, Natural Sciences Department
Sidney R. Hemming ORCID:0000-0001-8117-2303
Lamont Doherty Earth Observatory
Geochemistry Division
Columbia University
Department of Earth and Environmental Science

Ian R. Hall ORCID: 0000-0001-6960-1419

Cardiff University
School of Earth and Ocean Sciences
Leah J. LeVay ORCID: 0000-0003-3031-7079
Texas A&M University
International Ocean Discovery Program
Stephen Barker ORCID: 0000-0001-7870-6431
Cardiff University
School of Earth and Ocean Sciences

Luis Tejada

Hostos Community College
Physical Sciences Unit, Natural Sciences Department

Margit H. Simon

NORCE Norwegian Research Centre
Bjerknes Centre for Climate Research

Expedition 361 Scientists

Keywords: Expedition 361, South African Climates, Site U1474, Natal Valley, Agulhas

Current, Geochemistry, XRF Core Scanning

Data report: X-ray fluorescence core scanning of IODP Site U1474 sediments, Natal Valley, Southwest Indian Ocean

Daniel P. Babin ^{1, 2}, Allison M. Franzese ^{1, 3}, Sidney R. Hemming ^{1, 2}, Ian R. Hall ⁴, Leah J. LeVay ⁵, Stephen Barker ⁴, Luis Tejada³, Margit H. Simon ⁶, and Expedition 361 Scientists

1. Lamont-Doherty Earth Observatory
2. Department of Earth and Environmental Sciences, Columbia University
3. Physical Sciences Unit, Natural Sciences Department, Hostos Community College,
4. School of Earth and Ocean Sciences, Cardiff University, United Kingdom
5. International Ocean Discovery Program
6. NORCE Norwegian Research Centre, Bjerknes Centre for Climate Research

Abstract

X-ray fluorescence core scanning was conducted on International Ocean Discovery Program Site U1474, located in the Natal Valley off the coast of South Africa. The data, collected at a 2 mm resolution along the 255 m length of the splice, but these settings resulted in noisy data. This problem was addressed by applying a 10-point running sum on the XRF data prior to converting peak area to intensities. This effectively integrates 10 measurements into one and significantly improves noise in the data. With 25 calibration samples, whose element concentrations were derived using ICP-OES, the XRF measurements were converted to concentrations using the Univariate Log-Ratio Calibration of Weltje & Tjallingii (2008). The resulting concentrations of terrigenously derived major elements (Al, Si, K, Ti, and Fe) are

anti-correlated with Ca concentrations, indicating the main control on sediment chemistry is the variable proportions of terrigenous to in situ produced carbonate material.

1.0 Introduction

XRF core-scanning is widely used in paleoceanography and provides qualitative, high-resolution, direct geochemical measurements along the length of a sediment or rock core. While log-ratios represent well the sense of variability in the data, there is a clear advantage to calibrating XRF data (Weltje, 2002; Weltje et al., 2015; Weltje & Tjallingii, 2008), which enables direct comparison to geochemical data gathered with other methods. The calibration process involves subsampling along the length of the core, determining absolute elemental concentrations using a different geochemical method, such as inductively-coupled plasma mass spectrometry, and comparing these values to the counts derived by XRF.

International Ocean Discovery Program (IODP) Expedition 361 (South African Climates) Site U1474 was drilled 88 nmi southwest of Durban, South Africa, at 31°13.00'S; 31°32.71'E and 3045 m below sea level and produced a record going back to at least 6 Ma (Hall et al., 2017)(Figure 1). The site is located in the path of the Agulhas Current, a large western boundary current (70 Sv) flowing south along Africa's southeast margin (Lutjeharms, 2006). The record was obtained with the intention of documenting changes in both Agulhas Current variability and southern African paleoclimate. The composition of sediment at Site U1474 is largely terrigenous (55-65%) and clay abundance is high (Hall et al., 2017). Likely terrigenous sediment contributors include river systems proximal to the core site, such as the Tugela, Mfolozi, and Mkumazi Rivers, which drain the nearby Drakensberg Mountains (Hall et al., 2017; Simon et al., 2015) (Figure 1). The Natal Valley receives sedimentation from

more distant sources, such as the Limpopo and Zambezi Rivers. This is known because the >63 um fraction of Natal Valley sediment has a high $^{87}\text{Sr}/^{86}\text{Sr}$ ratio, reflecting the Archean age of the Kaapvaal and Zimbabwe Cratons eroded by the Zambezi and Limpopo (Franzese et al., 2006, 2009)(Figure 1). Sediment from these rivers is presumably transported to the Natal Valley via the Mozambique Current, estimated today to have a 15 Sv flux (Ridderinkhof et al., 2010)(Figure 1) and ultimately the Agulhas Current.

Work conducted by Simon et al. (2015) at the pre-cruise site (CD-154-10-06P, $31^{\circ}10.36' \text{ S}$, $032^{\circ} 08.91' \text{ E}$, 3076 m water depth) used the Fe/K ratio of bulk sediment, derived by XRF core scanning, to monitor the changing character of the terrigenous fraction. Because K is more mobile during weathering than Fe (Kossoff et al., 2012) and the spatial distribution of Fe and K in surface marine sediments tends to reflect the wetness or dryness of proximal sediment sources, (Govin et al., 2012), they argued the changing Fe/K ratio to indicate changes in chemical weathering a consequence of changing hydroclimatic conditions (Simon et al., 2015). Simon et al. (2015) found precessional variation in the intensity of chemical weathering of sediment, consistent throughout the 270 ky length of the record (Simon et al., 2015). A similar application of XRF core scanning on the 6 My record at U1474 could be useful in monitoring hydroclimate on longer timescales.

2.0 Methods and Materials

2.1 Data Collection

2.1.1 XRF Core Scans

An ITRAX Core Scanner (Croudace et al., 2006) in the Core Repository at Lamont-Doherty Earth Observatory was used to scan 213 sections (archive halves), composing the U1474

splice. Each section was removed from refrigeration 30 minutes before measurement to allow the core to warm to room temperature. Surface roughness was removed from the core with a plastic card, and the core was covered with 4 μm thick Ultralene plastic film (SPEX Centriprep, Inc.) before being placed on the scanner, which is essential to minimize variation in parameter S in the XRF calibration (Weltje & Tjallingii, 2008). Warming before adding the film helps prevent condensation on the film. Condensation absorbs X-Ray spectra, especially biasing light elements (Kido et al., 2006). X-ray illumination area was set at 2 mm in the down core direction and 2 cm in the cross-core direction, and the scan was run down the center of the split core half. Measurement spacing was set at 2 mm, the voltage at 30 kV, and the amperage at 55 mA, with an exposure time of 2 seconds using a Cr tube.

Due to shipping error, one core (U1474E-17H; Sections 1-3; Splice Depth CCSF 221.61 – 225.50 m) did not reach Lamont-Doherty Earth Observatory. Consequently, data from this interval is missing.

2.1.2 Calibration Samples

Discrete 10 cm^3 samples were taken from the working halves for (non-destructive) shipboard measurements of moisture and density (MAD). Because water content is one of the key variables that affects measured XRF intensities, we used a subset of the MAD sample residues for this calibration. After the XRF scanning was complete, we selected 23 of the MAD residues to capture the range of variability seen in the XRF scan data. Because the MAD samples were not necessarily taken from sections included in the splice, we used the magnetic susceptibility records to tie each MAD sample to a precise depth interval on the archive halves that were used for scanning (Table 1). The 25 discrete samples were digested using a standard lithium metaborate flux fusion method along with a set of six

powdered rock standards and six procedural blanks. Element concentrations were measured by Inductively Coupled Plasma-Optical Emission Spectrometry (ICP-OES) using the Agilent 720 axial ICP-OES at the Lamont Doherty Earth Observatory-American Museum of Natural History ICPMS Lab, for which routine precision is 1-2%. Signal intensities were corrected for blanks and instrumental drift, then converted to concentrations using the accepted values for the six rock standards (Table 2). The raw data and data reduction process for calculating elemental concentrations for the calibrations samples is documented in an interactive notebook format on

https://github.com/danielbabin/U1474_XRF_Data_Report/blob/master/Notebooks/xrf calibration samples reduction.ipynb

2.1.3 Calcium Carbonate Percent

An aliquot of the bulk moisture and density samples was powdered and measured for %CaCO₃ using a UIC CM5012 CO₂ Coulometer at Lamont Doherty Earth Observatory's Core Repository. Precision is determined is determined to be <4% by replicate measurements every 10 samples. These measurements of CaCO₃% are combined with measurements of CaCO₃ performed aboard the *JOIDES Resolution*. These data are listed in Table 3.

2.2 XRF Data Processing

2.2.1 Pre-Processing: Running Sum Spectra

For this study, we focus only on the major elements detectable with the ITRAX Al, Si, K, Ca, Ti, and Fe. Unfortunately, even for the major elements, the low dwell times chosen (2 seconds) yielded noisy records, especially for light elements like Al (Figure 3). Two seconds is the minimum recommended dwell time with the ITRAX Core Scanner. We chose this short dwell time, applied at a high resolution (2 mm), because we had a huge volume of core to

analyze and limited funds for analysis time. Fortunately, however, our high-resolution scanning allows us to integrate the raw spectral data across a wider depth interval, increasing the height of our spectra, and improving the signal-noise ratio.

To accomplish this, we access the raw spectral data, in the form of an “.spe” file, created with each measurement. The file contains a single vector of intensities at different energy wavelengths. We import all the spectral intensities from each “.spe” file (~750 for 1.5 m of core) from a single section into a data structure, and take a 10-measurement running sum at each energy level across that data structure. Taking a 10-measurement running sum across these data, collected every 2 mm for 2 seconds, simulates a 2 cm exposure for 20 seconds. This process is repeated for the 213 sections scanned. Some sections had measurements with very low total spectra intensities (the sum of each element in the spectra). These resulted from measuring air before or after sections or cracks in the core. All measurements with total spectral intensities lower than 300,000 were dropped for this reason. The Python code used these steps is available on GitHub in an interactive notebook format at

https://github.com/danielbabin/U1474_XRF_Data_Report/blob/master/Notebooks/xrf_processing.ipynb

For the ITRAX core scan, converting a spectra of energy intensities to element intensities involves fitting the observed spectra from a measurement with a model and computing the relevant area under the spectral peaks. This is done using the software Q-Spec, provided by ITRAX and Cox Analytical Systems for XRF Data Reduction (Croudace et al., 2006). To optimize the fit for several measurements (for example, along the length of a core section), the ITRAX software sums the spectra from each measurement in a core and outputs a

“sumspectra” .spe file. To optimize the model fit for our 213 sections, we averaged the intensities of our 213 sumspectra files. This average sumspectra was then fit using the Q-spec software. We chose elements for the spectral model that minimized mean-squared error (“MSE”). The parameters “keV/channel,” “energy offset,” “FWHM slope,” “FWHM offset,” and “FWHM cutoff” were also optimized to minimize MSE. We found that this method provides the highest quality record of element-intensity continuity in depth-space, minimizing jumps between sections. The MSE parameter provides a continuous assessment of how well the model fits each measurement. The full suite of elements measured can be found in the pre-processed XRF data (Table 5). The Q-spec settings file, a “.dfl” file type, we used for our data reduction can be found in the supplemental information.

Section positions were converted into core depth (Core depth below seafloor: CSF-A), then put on U1474 splice depth (core composite depth below seafloor: CCSF). No pre-processing steps, outlier removal, or filtering were necessary beyond the steps previously mentioned. The final result is XXXX measurements of elemental intensities along ~250 m of core. While we only focus on major elements – Al, Si, K, Ca, Ti, and Fe – an extensive suite of elements not suitable for calibration are available in the raw XRF data. Table 4 contains the 2 mm-2 second XRF data. Table 5 contains the 2 cm-20 second integrated XRF dataset.

The raw XRF data in depth series can be visualized in Figure 3 and Figure 4. Figure 3 shows individual element intensities for both the 2 cm-20 second dataset (full color) and the 2 mm-2 second (paler colors) dataset. Figure 4 presents element intensities from both datasets normalized to Ca intensity. This set of figures clearly visualizes the improvement in noise reduction offered by the 2 cm integration of the raw spectra.

2.3 XRF Core-Scan Calibration to Concentrations

The relative abundances provided by the XRF, in “counts,” were converted to concentrations with a calibration dataset of 25 samples (Table 6, Figures 5 and 6). The conversion was made using the Univariate Log-ratio Calibration (ULC) of (Weltje & Tjallingii, 2008), with Ca counts and concentrations in the denominator of each element ratio. We chose the simpler ULC as opposed to the more sophisticated Multi-variate Log-ratio Calibration (MLC) of Weltje et al. (2015) due to the relative sparse spacing of our calibration samples compared to the total length of our core. Concentrations for the calibration are reported in oxides. The Python code used for the calibration process, including the calculation of α and β parameters, is available in an interactive notebook format at

https://github.com/danielbabin/U1474_XRF_Data_Report/blob/master/Notebooks/xrf_calibrator.ipynb. Model parameters α and β are available in Table 7.

The ULC is designed to calibrate element ratios, not necessarily individual element concentrations. But, if the elements in the collection of ratios is assumed to compose the entire sample, the relative concentrations of each element can be calculated. To ensure the resulting XRF-core-scan-derived concentrations reflect the concentrations of our calibration samples as closely as possible, we normalize the sum of the each calibrated XRF measurement to 96.2%, the average sum of $\text{Al}_2\text{O}_3 + \text{SiO}_2 + \text{K}_2\text{O} + \text{CaO} + \text{TiO}_2 + \text{Fe}_2\text{O}_3$ in the 25 calibration samples. This simply reflects the fact that the XRF did not measure Na_2O and MgO , which sum to 3.8 % on average in the calibration dataset.

The results of the calibration in depth series can be visualized in Figure 4 and Figure 5. Figure 4 shows individual element intensities. Figure 5 presents element intensities from both

datasets normalized to Ca intensity. Black circles along each depth series are the concentrations and element ratios from the calibration samples.

3.0 Results

3.1 Data Quality

Figure 3, showing individual element intensities, indicates a few sections with unusually low counts, highlighted with grey bars (U1474D-4H-1A, U1474D-8H-3A, U1474D-11H-4A, U1474D-11H-5A). We attribute these anomalous sections to malfunctions with the ITRAX scanner. The sections cannot be rescanned because these anomalous sections were not discovered until the cores were shipped away from Lamont-Doherty. However, while counts of individual element intensities are affected by this malfunction, ratios seem less affected (Figure 4, Figure 6). Ratios from core sections are joined together, making a continuous depth-series (Figure 6). As ratios are the typical application of XRF data, we argue these sections may be used with caution.

Figure 7 follows the calibration process by comparing the calibration samples with the XRF measurements at the appropriate depth. Figure 7A compares the ratios of the raw counts. Figure 7B compares the log-ratios of the calibration and the XRF counts. Figure 7C compares ratios of the results, the calibrated XRF ratios. For each element ratio, there is a strong correlation with an intercept at zero, within boot-strapped uncertainty.

As mentioned previously, the ULC works best for ratios, but individual element concentrations can be derived if the collection of ratios is assumed to compose the entire sample, summed, and normalized. Figure 8 shows how effectively our calibration yielded individual element calibrations. Most elements have high quality calibrations, with R^2 coefficients greater than 0.53, and intercepts at or near zero within bootstrapped

uncertainty intervals. While titanium counts have a strong relationship with concentrations from the calibration sample, the relationship with XRF-derived concentrations is weaker. We make the pre-processed XRF data (counts) at 2-mm resolution, the running-spectral-sum XRF data (counts) at 2 cm resolution, and calibrated XRF data (major element oxides) in online tables Table 4, Table 5, and Table 6.

3.2 Description of Results

For marine sediment, CaO concentration at U1474 is low, ranging from 13-41% (Figure 4D). CaO concentration derived CaCO_3 coulometry Table 3 are plotted alongside the XRF data as white squares (Figure 4D), and the CaO concentration from both methods at identical depths is cross plotted in Figure 9. The results indicate that most of the Ca is borne within CaCO_3 . By calculating difference between total CaO and CaCO_3 borne CaO for each sample, we estimate an average terrigenous CaO content of approximately 5%. CaO abundance is lowest between 100-170 m CCSF. There is a large excursion toward high CaO deposition between 10-20 m core depth.

Elements derived from the continental crust, borne in terrigenous phases, vary inversely with Ca content (Figure 4A, B, C, E, F). The element with the greatest variability in the core scan dataset is K (Figure 4C), varying by more than a factor of 2 through the core. From 250-175 m CCSF, K content is low, compared to the rest of the record, about 1.25%, (Figure 4C). From 170-100 m CCSF, K increases to ~1.75%, overprinted by two low frequency excursions to even higher values. From 100-20 m CCSF, K concentration declines gradually to a minimum of ~.75 %. After this interval, K% increases again. Long term trends in variability of the other terrigenously derived elements – Al, Si, Ti, and Fe – largely follow the pattern for K described above (Figure 4A, B, E, F). The covariance of the terrigenously-derived elements

and anti-correlation of calcium carbonate indicates that the main control on the chemical composition of sediment at Site U1474 is the variable input of terrigenous material.

Acknowledgments

This research used samples and/or data provided by the International Ocean Discovery Program (IODP). We thank the International Ocean Drilling Program and the Expedition 361 sailing scientists and staff for the collection of core material. Funding for XRF scanning was provided by IODP. The staff operating the ITRAX core scanner at the Lamont-Doherty Earth Observatory Core Repository, Clara Chang and Nicole Anest, were extremely helpful in the XRF data collection process. We thank individuals from Lamont Doherty Earth Observatory's Climate and Life (2016) High School Intern Program: Andrew T. Celli, Elmina David, Ayla K. Markowski, Sonja O'Brien, Taiya Sharif, and Tess N. Strohm who aided with the long hours of core scanning. We thank an anonymous reviewer for their helpful input.

References

- Croudace, I. W., Rindby, A., & Rothwell, R. G. (2006). ITRAX: description and evaluation of a new multi-function X-ray core scanner. *Geological Society, London, Special Publications*, 267(1), 51 LP – 63. <https://doi.org/10.1144/GSL.SP.2006.267.01.04>
- Flanagan, F. J. (1984). *Three USGS mafic rock references samples, W-2, DNC-1, and BIR-1*.
- Franzese, A. M., Hemming, S. R., Goldstein, S. L., & Anderson, R. F. (2006). Reduced Agulhas Leakage during the Last Glacial Maximum inferred from an integrated provenance and flux study. *Earth and Planetary Science Letters*, 250(1), 72–88.
<https://doi.org/https://doi.org/10.1016/j.epsl.2006.07.002>
- Franzese, A. M., Hemming, S. R., & Goldstein, S. L. (2009). Use of strontium isotopes in detrital sediments to constrain the glacial position of the agulhas retroflection. *Paleoceanography*.

<https://doi.org/10.1029/2008PA001706>

Govin, A., Holzwarth, U., Heslop, D., Ford Keeling, L., Zabel, M., Mulitz, S., et al. (2012).

Distribution of major elements in Atlantic surface sediments (36°N–49°S): Imprint of terrigenous input and continental weathering. *Geochemistry, Geophysics, Geosystems*, 13(1).

Hall, I. R., Hemming, S. R., LeVay, L. J., Barker, S., Berke, M. A., Brentegani, L., et al. (2017). Site U1474, 361(September). <https://doi.org/10.14379/iodp.proc.361.103.2017>

Imai, N., TERASHIMA, S., ITOH, S., & ANDO, A. (1996). 1996 COMPILATION OF ANALYTICAL DATA ON NINE GSJ GEOCHEMICAL REFERENCE SAMPLES, “SEDIMENTARY ROCK SERIES.” *Geostandards Newsletter*, 20(2), 165–216.

<https://doi.org/10.1111/j.1751-908X.1996.tb00184.x>

Kido, Y., Koshikawa, T., & Tada, R. (2006). Rapid and quantitative major element analysis method for wet fine-grained sediments using an XRF microscanner. *Marine Geology*, 229(3), 209–225. <https://doi.org/https://doi.org/10.1016/j.margeo.2006.03.002>

Kossoff, D., Hudson-Edwards, K. A., Dubbin, W. E., & Alfredsson, M. (2012). Major and trace metal mobility during weathering of mine tailings: Implications for floodplain soils. *Applied Geochemistry*, 27(3), 562–576.

<https://doi.org/https://doi.org/10.1016/j.apgeochem.2011.11.012>

Lutjeharms, J. R. E. (2006). *The agulhas current. The Agulhas Current.*
<https://doi.org/10.1007/3-540-37212-1>

McLennan, S. M., & Taylor, S. R. (1980). Geochemical standards for sedimentary rocks: Trace-element data for U.S.G.S. standards SCo-1, MAG-1 and SGR-1. *Chemical Geology*, 29(1–

4), 333–343. [https://doi.org/10.1016/0009-2541\(80\)90029-7](https://doi.org/10.1016/0009-2541(80)90029-7)

Pretorius, W., Weis, D., Williams, G., Hanano, D., Kieffer, B., & Scoates, J. (2006). Complete Trace Elemental Characterisation of Granitoid (USGS G-2, GSP-2) Reference Materials by High Resolution Inductively Coupled Plasma-Mass Spectrometry. *Geostandards and Geoanalytical Research*, 30(1), 39–54. <https://doi.org/10.1111/j.1751-908X.2006.tb00910.x>

Ridderinkhof, H., Werf, P. M. Van Der, Ullgren, J. E., Aken, H. M. Van, Leeuwen, P. J. Van, & Ruijter, W. P. M. De. (2010). Seasonal and interannual variability in the Mozambique Channel from moored current observations, 115. <https://doi.org/10.1029/2009JC005619>

Simon, M. H., Ziegler, M., Bosmans, J., Barker, S., Reason, C. J. C., & Hall, I. R. (2015). Eastern South African hydroclimate over the past 270,000 years. *Scientific Reports*. <https://doi.org/10.1038/srep18153>

Weltje, G. J. (2002). Quantitative analysis of detrital modes: statistically rigorous confidence regions in ternary diagrams and their use in sedimentary petrology. *Earth-Science Reviews*, 57(3–4), 211–253.

Weltje, G. J., & Tjallingii, R. (2008). Calibration of XRF core scanners for quantitative geochemical logging of sediment cores: Theory and application. *Earth and Planetary Science Letters*. <https://doi.org/10.1016/j.epsl.2008.07.054>

Weltje, G. J., Bloemsma, M. R., Tjallingii, R., Heslop, D., Röhl, U., & Croudace, I. W. (2015). Prediction of geochemical composition from XRF core scanner data: a new multivariate approach including automatic selection of calibration samples and quantification of uncertainties. In *Micro-XRF Studies of Sediment Cores* (pp. 507–534). Springer.

Figures

Figure 1:

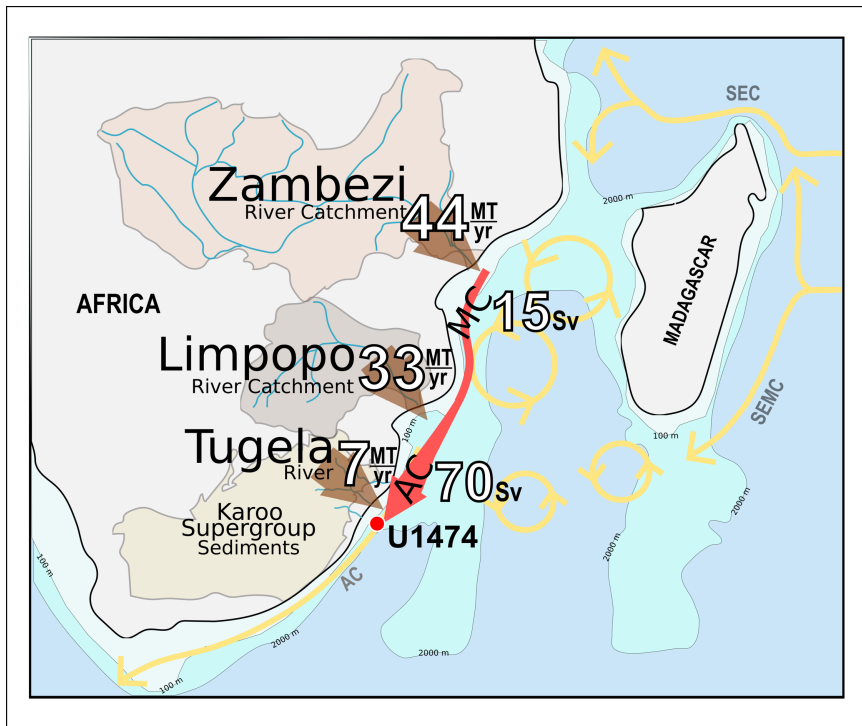


Figure 2:

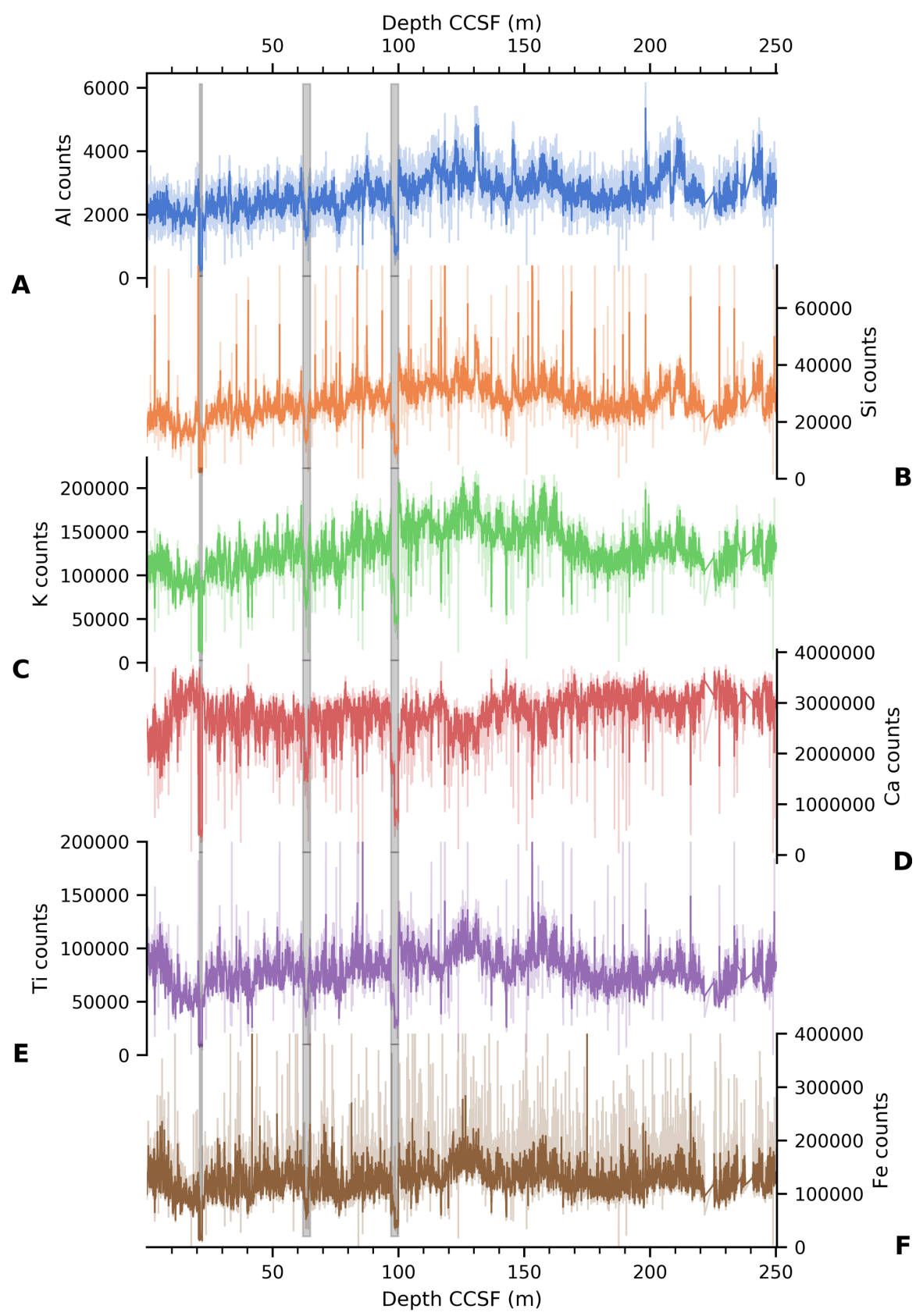


Figure 3:

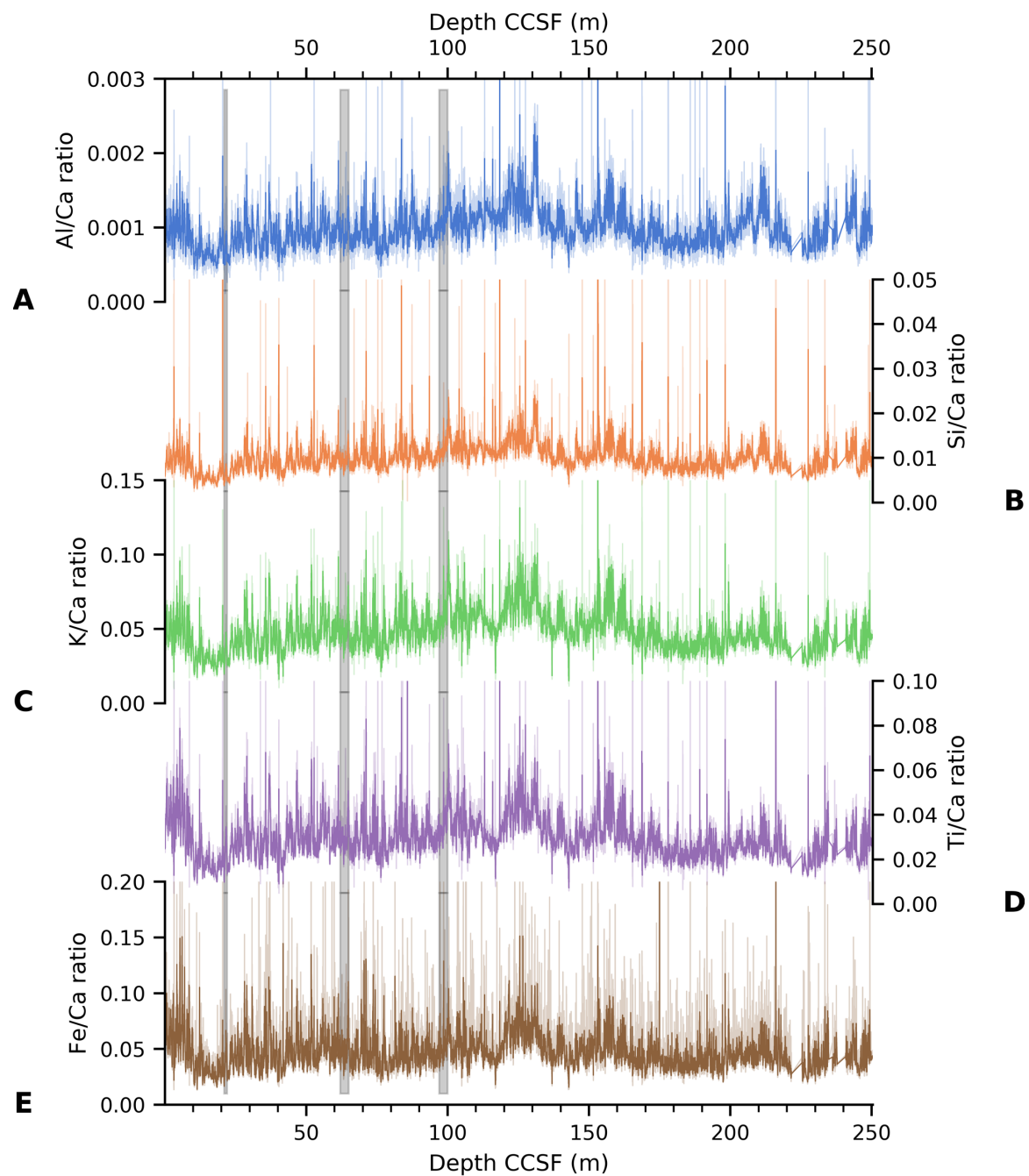


Figure 4:

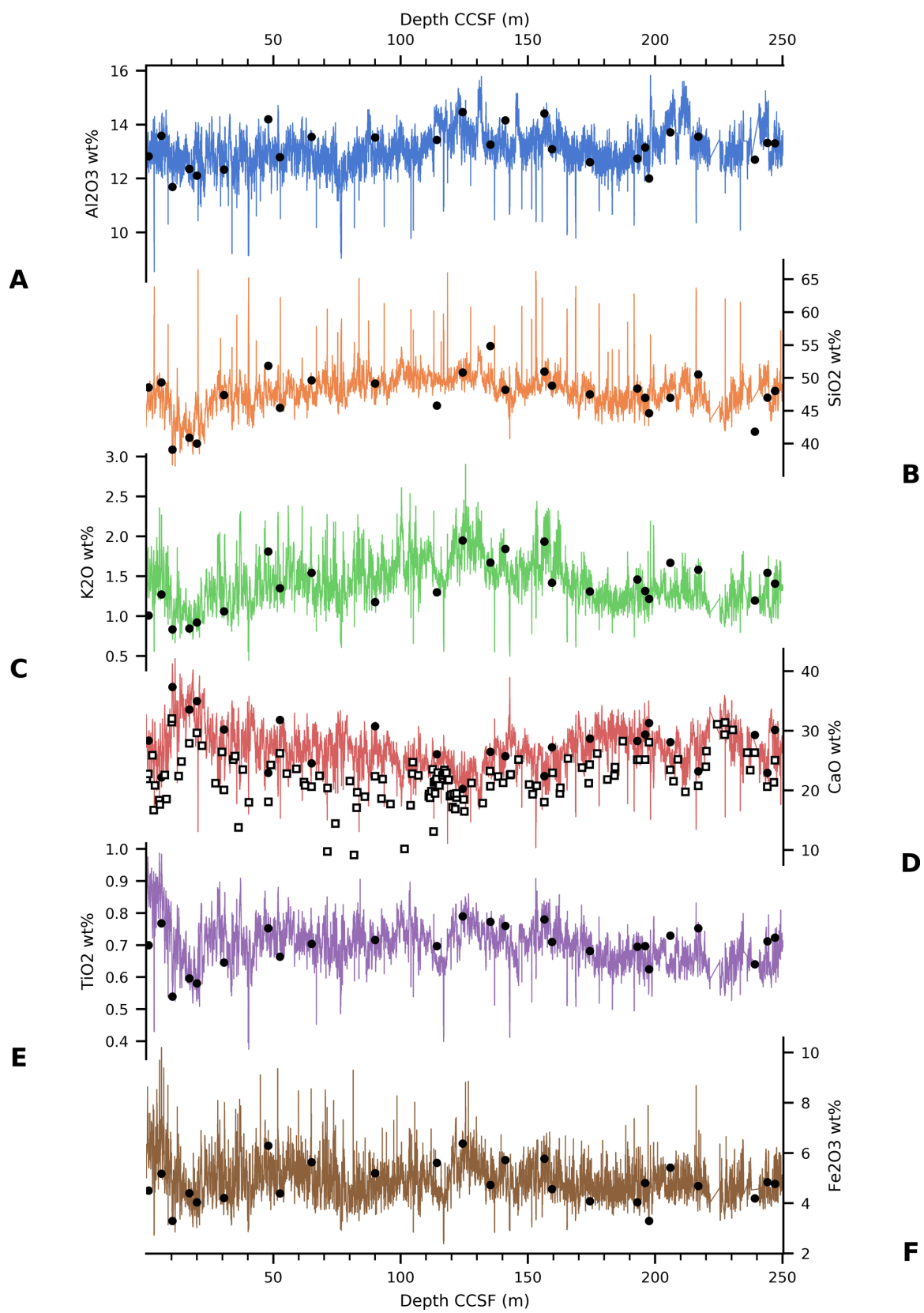


Figure 5:

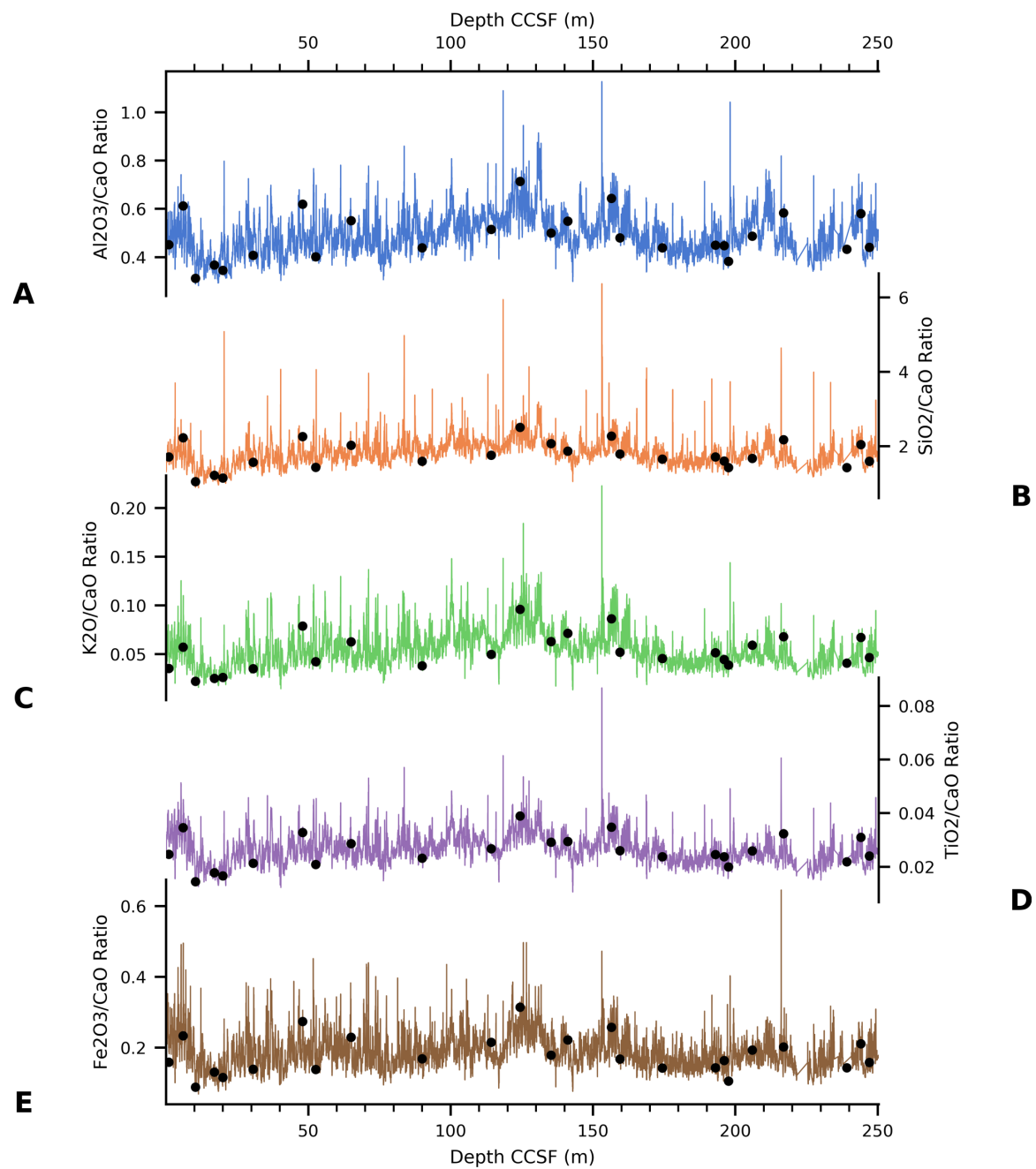


Figure 6:

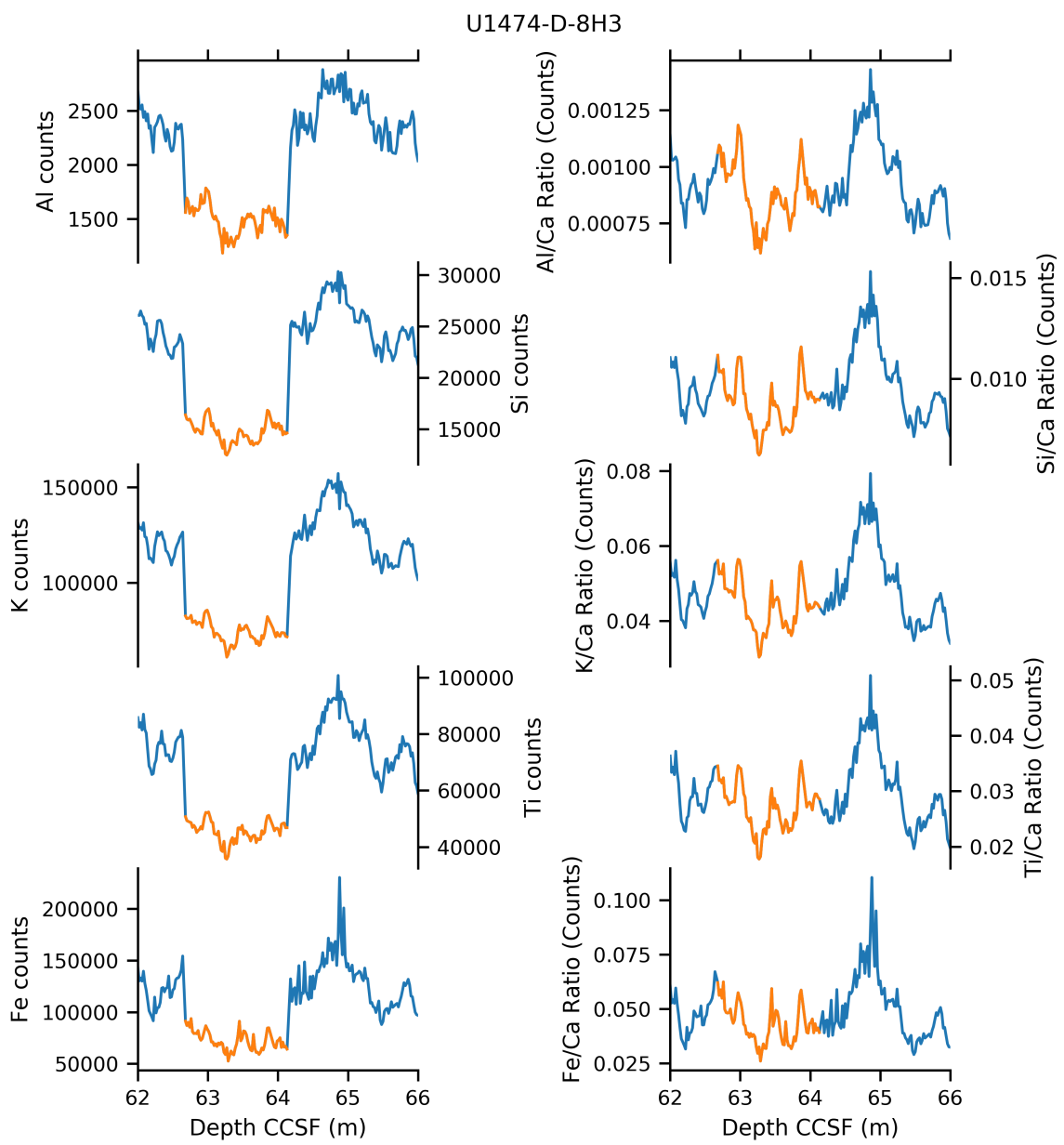


Figure 7:

Univariate Log-Ratio Calibration Process

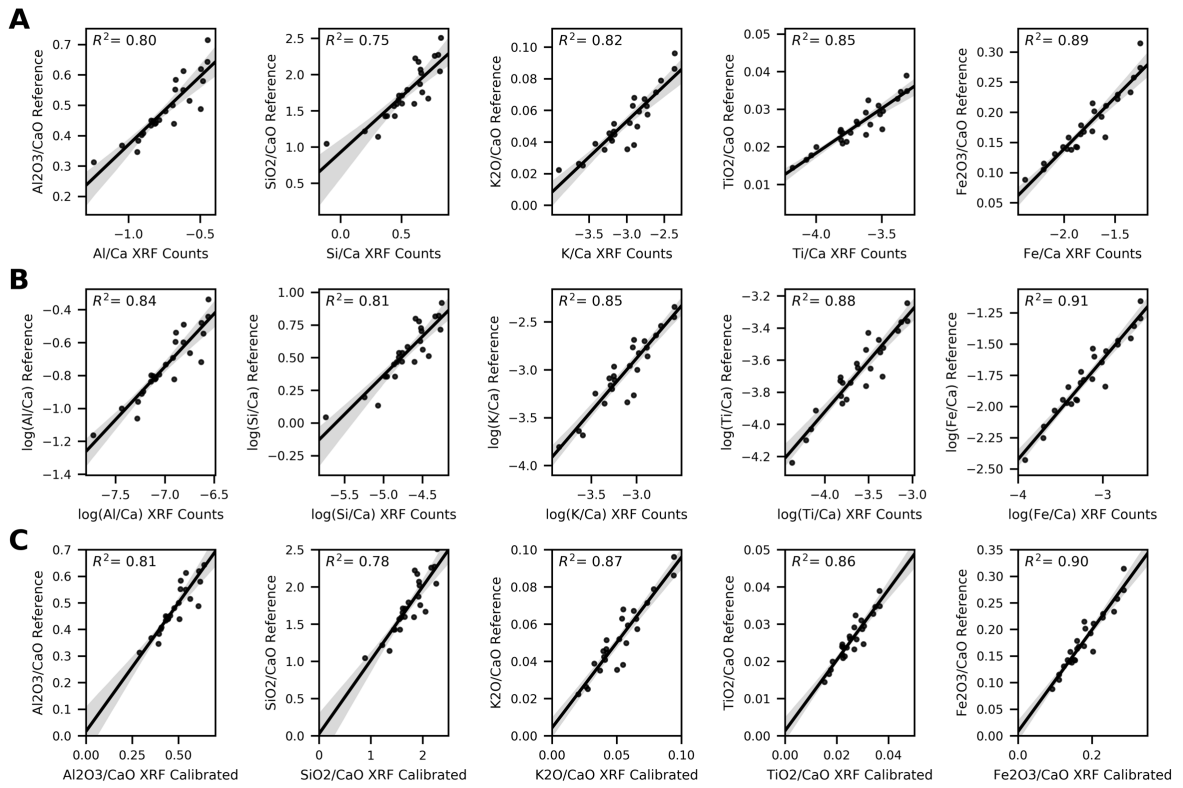


Figure 8:

Calibration Samples vs XRF Data Before and After Univariate Log-Ratio Calibration

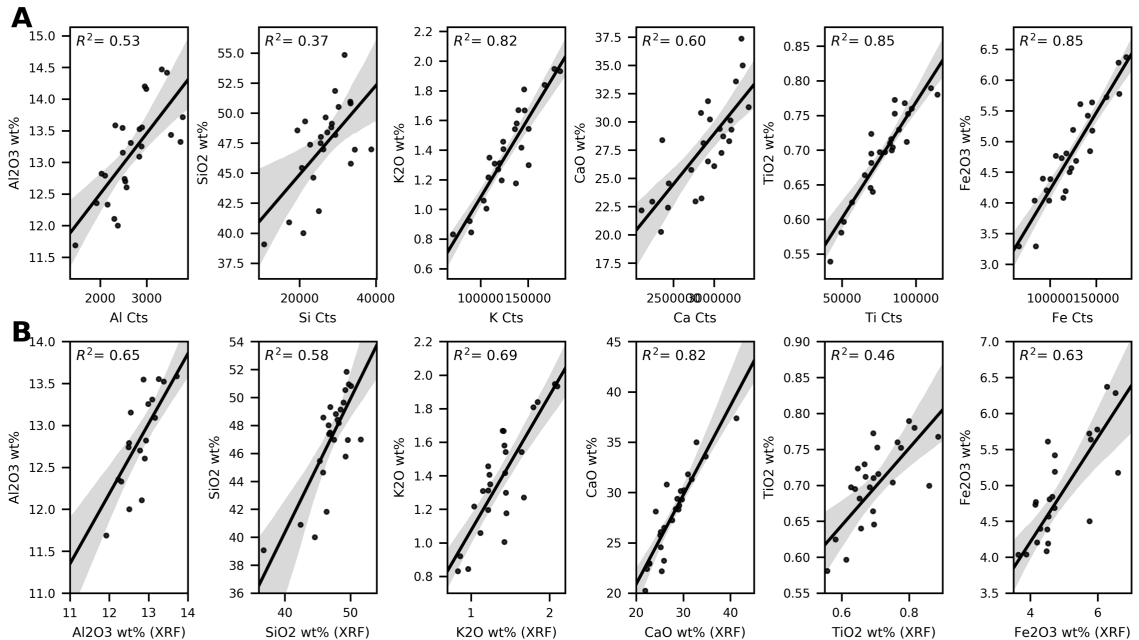


Figure 9:

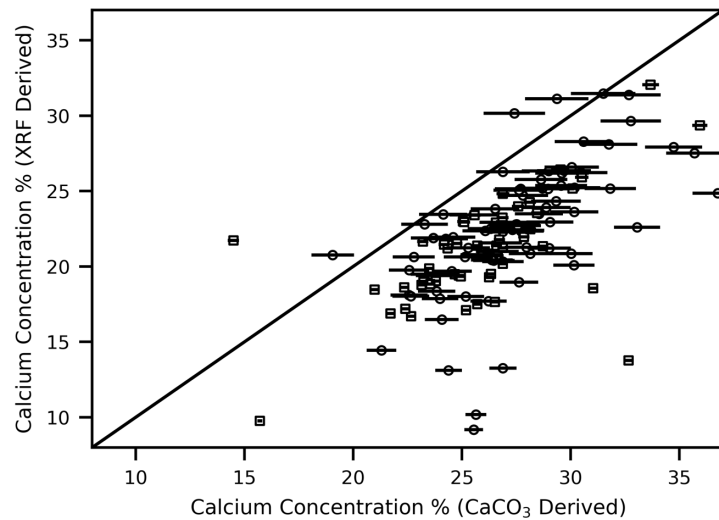


Figure captions

Figure 1:

Drainage configuration and oceanography of Southern Africa. The Zambezi and Limpopo are Africa's largest rivers draining into the Indian Ocean, Draining 44 and 33 Mt of sediment annually (white numbers)[Milliman and Meade, 1983]. Sediment from those rivers would be transported to U1474 first by the Mozambique Channel eddies transporting 15 Sv (Ridderenckoff et al., 2010), and ultimately via the strong Agulhas Current (Lutjeharms, 2006). The Tugela River and other, smaller rivers, drain the Drakensberg mountains, flanking the southeastern African Margin. The mountains are composed of dominantly sedimentary rock of Paleozoic age, called the Karoo Supergroup [Johnson et al., 1996]. NV= Natal Valley. AC= Agulhas Current. SEMC = Southeast Madagascar Current. SEC = South Equatorial Current.

Figure 2:

The raw XRF data in depth series for each element. The series in the background with pale colors come from the 2 mm-2 sec dataset. In the foreground, in dark colors, are the data from the integrated 2 cm-20 sec dataset. Elements are A) Aluminum, B) Silicon, C) Potassium, D) Calcium, E) Titanium, F) Iron. Grey bars highlight the four sections with anomalously low counts.

Figure 3:

The raw XRF data in depth series for each element, but each element is normalized by Ca counts. The series in the background with pale colors come from the 2 mm-2 sec dataset. In the foreground, in dark colors, are the data from the integrated 2 cm-20 sec dataset. Ratios are A) Al/Ca, B) Si/Ca, C) K/Ca, D) Ti/Ca, E) Fe/Ca. Grey bars highlight the same four sections with anomalously low counts. The sections do not stand out when presented in ratio form (see figure 6).

Figure 4:

The calibrated XRF data in depth series for each element. Black circles are the concentrations of the calibration samples. Elements are A) Aluminum, B) Silicon, C) Potassium, D) Calcium, E) Titanium, F) Iron. Data are presented in wt% oxide.

Figure 5:

The calibrated XRF data in depth series for each element ratio, normalized to CaO. Black circles are the concentrations of the calibration samples. Ratios are A) Al₂O₃/CaO, B) SiO₂/CaO, C) K₂O/CaO, D) TiO₂/CaO, E) Fe/Ca. Data are expressed in wt% oxide.

Figure 6:

The ITRAX scanner experienced problems during the scans of four cores: D-4H-1, D-8H-3, D-11H-4, and D-11H-5. Here we use the depth series from D-8H-3 to demonstrate how the ratios from the problematic sections appear usable.

Figure 7:

A comparison of the counts derived from the XRF spectra to the ratioed concentrations from the calibration samples after each step in the XRF data reduction procedure provides a quality check. A) 2 cm-20 sec dataset, unprocessed B) Logged ratios of both concentrations and counts C) Calibrated ratios.

Figure 8:

A comparison of the XRF data to calibration samples using individual element concentrations A) before calibration and, B) after the calibration.

Figure 9:

The comparison of CaO concentration derived by XRF core scanning and CaO concentration calculated from %CaCO₃ abundance. Squares are measurements from the JOIDES Resolution. Circles are from this study. Error bars represent precision at 1 standard deviation, estimated by replicates. In black is the 1:1 line.

Tables

Table 1: List of discrete samples used for calibrating XRF concentrations

| Exp | Site | Hole | Core | Type | Section | A/W | Top Offset (cm) | Top Depth (m CSF-A) | Top Depth (m CCSF*) |
|-----|-------|------|------|------|---------|-----|--------------------|------------------------|------------------------|
| 361 | U1474 | A | 1 | H | 1 | W | 92 | 0.92 | 1 |
| 361 | U1474 | A | 2 | H | 5 | W | 20 | 11.6 | 10.365 |
| 361 | U1474 | A | 3 | H | 3 | W | 76 | 18.66 | 16.963 |

| | | | | | | | | | |
|-----|-------|---|----|---|---|---|-----|--------|---------|
| 361 | U1474 | A | 3 | H | 5 | W | 76 | 21.66 | 19.963 |
| 361 | U1474 | A | 4 | H | 4 | W | 113 | 30.03 | 30.626 |
| 361 | U1474 | A | 6 | H | 2 | W | 77 | 45.67 | 48.03 |
| 361 | U1474 | A | 6 | H | 5 | W | 84 | 50.24 | 52.61 |
| 361 | U1474 | A | 7 | H | 7 | W | 52 | 62.42 | 65.06 |
| 361 | U1474 | A | 12 | H | 4 | W | 104 | 105.97 | 114.225 |
| 361 | U1474 | A | 13 | H | 4 | W | 106 | 115.47 | 124.37 |
| 361 | U1474 | A | 14 | H | 4 | W | 102 | 124.92 | 135.234 |
| 361 | U1474 | A | 15 | H | 2 | W | 106 | 131.47 | 141.095 |
| 361 | U1474 | A | 16 | H | 6 | W | 102 | 146.92 | 156.46 |
| 361 | U1474 | A | 17 | H | 2 | W | 102 | 150.42 | 159.46 |
| 361 | U1474 | A | 18 | H | 4 | W | 101 | 162.91 | 174.3 |
| 361 | U1474 | A | 20 | H | 2 | W | 96 | 178.86 | 193.015 |
| 361 | U1474 | A | 20 | H | 4 | W | 97 | 181.87 | 196.025 |
| 361 | U1474 | A | 20 | H | 5 | W | 102 | 183.41 | 197.565 |
| 361 | U1474 | A | 21 | H | 2 | W | 106 | 188.46 | 205.957 |
| 361 | U1474 | A | 22 | H | 2 | W | 102 | 197.92 | 216.915 |
| 361 | U1474 | A | 24 | H | 4 | W | 110 | 219.97 | 230.415 |
| 361 | U1474 | A | 25 | H | 2 | W | 102 | 224.51 | 236.184 |
| 361 | U1474 | A | 25 | H | 4 | W | 102 | 227.52 | 247.04 |

Table 2: Bulk sediment composition of U1474 MAD residues

| Sample | Depth CCSF (m) | Depth CCSF | | | | | | Cu | Fe2O3 |
|-----------|-------------------|------------|--------|-------|--------|--|--|-------|-------|
| | | Al2O3 | Ba | CaO | Cr | | | | |
| 1474 1H1 | 1.00 | 12.82 | 586.67 | 28.38 | 123.75 | | | 14.14 | |
| 1474 2H1 | 5.99 | 13.59 | 625.10 | 22.18 | 148.87 | | | 32.43 | |
| 1474 2H5 | 10.37 | 11.69 | 451.47 | 37.37 | 92.72 | | | 32.27 | |
| 1474 3H3 | 16.96 | 12.36 | 473.26 | 33.59 | 113.27 | | | 18.16 | |
| 1474 3H5 | 19.96 | 12.11 | 582.45 | 35.01 | 101.26 | | | 36.98 | |
| 1474 4H4 | 30.63 | 12.33 | 511.77 | 30.23 | 113.12 | | | 17.86 | |
| 1474 6H2 | 48.03 | 14.20 | 532.38 | 22.94 | 140.85 | | | 43.22 | |
| 1474 6H5 | 52.61 | 12.79 | 625.76 | 31.83 | 117.18 | | | 40.00 | |
| 1474 7H7 | 65.06 | 13.55 | 571.97 | 24.56 | 120.07 | | | 36.74 | |
| 1474 10H2 | 89.95 | 13.53 | 457.33 | 30.79 | 134.75 | | | 52.17 | |
| 1474 12H4 | 114.26 | 13.44 | 510.71 | 26.09 | 118.99 | | | 30.83 | |
| 1474 13H4 | 124.37 | 14.47 | 520.99 | 20.26 | 146.08 | | | 30.17 | |
| 1474 14H4 | 135.23 | 13.25 | 549.69 | 26.50 | 150.16 | | | 32.27 | |
| 1474 15H2 | 141.10 | 14.16 | 443.38 | 25.76 | 148.20 | | | 39.46 | |

| | | | | | | |
|-----------|--------|-------|--------|-------|--------|-------|
| 1474 16H6 | 156.46 | 14.42 | 493.34 | 22.41 | 139.11 | 35.78 |
| 1474 17H2 | 159.46 | 13.09 | 462.03 | 27.25 | 126.90 | 28.35 |
| 1474 18H4 | 174.30 | 12.61 | 425.89 | 28.72 | 124.00 | 27.40 |
| 1474 20H2 | 193.02 | 12.74 | 489.65 | 28.31 | 105.39 | 27.56 |
| 1474 20H4 | 196.03 | 13.16 | 422.64 | 29.38 | 146.25 | 28.16 |
| 1474 20H5 | 197.57 | 12.00 | 450.53 | 31.32 | 96.97 | 53.98 |
| 1474 21H2 | 205.96 | 13.72 | 467.55 | 28.13 | 145.85 | 34.15 |
| 1474 22H2 | 216.92 | 13.55 | 513.85 | 23.23 | 122.84 | 27.28 |
| 1474 24H4 | 239.15 | 12.70 | 469.80 | 29.32 | 112.01 | 31.43 |
| 1474 25H2 | 244.05 | 13.32 | 518.50 | 22.97 | 125.54 | 26.76 |
| 1474 25H4 | 247.04 | 13.31 | 562.31 | 30.15 | 125.20 | 28.93 |

Table 3: CaCO3% Measurements

| Depth CCSF (m) | Exp | Site | Hole | Core | Type | Sect | A/W | %C |
|-------------------|-----|-------|------|------|------|------|-----|----|
| 0.3 | 361 | U1474 | A | | 1 H | | 1 W | |
| 0.92 | 361 | U1474 | A | | 1 H | | 1 W | |
| 2.5 | 361 | U1474 | A | | 1 H | | 2 W | |
| 3.08 | 361 | U1474 | A | | 1 H | | 3 W | |
| 3.57 | 361 | U1474 | A | | 1 H | | 3 W | |
| 5.192 | 361 | U1474 | A | | 2 H | | 1 W | |
| 5.442 | 361 | U1474 | A | | 2 H | | 2 W | |
| 7.412 | 361 | U1474 | A | | 2 H | | 3 W | |
| 8.062 | 361 | U1474 | A | | 2 H | | 3 W | |
| 10.102 | 361 | U1474 | A | | 2 H | | 5 W | |
| 10.192 | 361 | U1474 | A | | 2 H | | 5 W | |
| 12.837 | 361 | U1474 | A | | 2 H | | 7 W | |
| 13.963 | 361 | U1474 | A | | 3 H | | 1 W | |
| 16.963 | 361 | U1474 | A | | 3 H | | 3 W | |
| 19.963 | 361 | U1474 | A | | 3 H | | 5 W | |
| 22.003 | 361 | U1474 | A | | 3 H | | 7 W | |
| 27.336 | 361 | U1474 | A | | 4 H | | 2 A | |
| 29.846 | 361 | U1474 | A | | 4 H | | 4 W | |
| 30.626 | 361 | U1474 | A | | 4 H | | 4 W | |
| 34.326 | 361 | U1474 | A | | 4 H | | 7 W | |
| 35 | 361 | U1474 | A | | 5 H | | 1 W | |
| 36.32 | 361 | U1474 | A | | 5 H | | 2 W | |
| 38 | 361 | U1474 | A | | 5 H | | 3 W | |

| | | | | | | | |
|---------|-----|-------|---|----|---|---|---|
| 40.39 | 361 | U1474 | A | 5 | H | 5 | W |
| 48.053 | 361 | U1474 | A | 6 | H | 2 | W |
| 48.993 | 361 | U1474 | A | 6 | H | 3 | W |
| 52.623 | 361 | U1474 | A | 6 | H | 5 | W |
| 55.322 | 361 | U1474 | A | 6 | H | 7 | W |
| 59.053 | 361 | U1474 | A | 7 | H | 3 | W |
| 62.013 | 361 | U1474 | A | 7 | H | 5 | W |
| 62.448 | 361 | U1474 | A | 7 | H | 5 | W |
| 65.033 | 361 | U1474 | A | 7 | H | 7 | W |
| 68.207 | 361 | U1474 | A | 8 | H | 2 | W |
| 71.217 | 361 | U1474 | A | 8 | H | 4 | W |
| 71.357 | 361 | U1474 | A | 8 | H | 4 | W |
| 74.357 | 361 | U1474 | A | 8 | H | 6 | W |
| 80.116 | 361 | U1474 | A | 9 | H | 2 | W |
| 81.686 | 361 | U1474 | B | 9 | H | 4 | W |
| 82.711 | 361 | U1474 | A | 9 | H | 4 | W |
| 83.011 | 361 | U1474 | A | 9 | H | 4 | W |
| 85.991 | 361 | U1474 | A | 9 | H | 6 | W |
| 89.97 | 361 | U1474 | A | 10 | H | 2 | W |
| 92.51 | 361 | U1474 | A | 10 | H | 4 | W |
| 92.97 | 361 | U1474 | A | 10 | H | 4 | W |
| 95.97 | 361 | U1474 | A | 10 | H | 6 | W |
| 103.914 | 361 | U1474 | A | 11 | H | 4 | W |
| 104.574 | 361 | U1474 | A | 11 | H | 4 | W |
| 104.768 | 361 | U1474 | B | 11 | H | 5 | W |
| 106.994 | 361 | U1474 | A | 11 | H | 6 | W |
| 111.089 | 361 | U1474 | F | 12 | H | 4 | W |
| 111.156 | 361 | U1474 | A | 12 | H | 2 | W |
| 111.589 | 361 | U1474 | F | 12 | H | 4 | W |
| 112.089 | 361 | U1474 | F | 12 | H | 5 | W |
| 112.589 | 361 | U1474 | F | 12 | H | 5 | W |
| 112.975 | 361 | U1474 | B | 12 | H | 4 | W |
| 113.149 | 361 | U1474 | F | 12 | H | 5 | W |
| 113.536 | 361 | U1474 | A | 12 | H | 4 | W |
| 113.589 | 361 | U1474 | F | 12 | H | 6 | W |
| 114.089 | 361 | U1474 | F | 12 | H | 6 | W |
| 114.176 | 361 | U1474 | A | 12 | H | 4 | W |
| 114.589 | 361 | U1474 | F | 12 | H | 6 | W |
| 115.139 | 361 | U1474 | F | 12 | H | 7 | W |
| 116.457 | 361 | U1474 | F | 13 | H | 1 | W |

| | | | | | | | |
|---------|-----|-------|---|----|---|---|---|
| 116.957 | 361 | U1474 | F | 13 | H | 1 | W |
| 117.236 | 361 | U1474 | A | 12 | H | 6 | W |
| 117.457 | 361 | U1474 | F | 13 | H | 1 | W |
| 117.957 | 361 | U1474 | F | 13 | H | 2 | W |
| 118.457 | 361 | U1474 | F | 13 | H | 2 | W |
| 118.957 | 361 | U1474 | F | 13 | H | 2 | W |
| 119.467 | 361 | U1474 | F | 13 | H | 3 | W |
| 119.967 | 361 | U1474 | F | 13 | H | 3 | W |
| 120.467 | 361 | U1474 | F | 13 | H | 3 | W |
| 120.997 | 361 | U1474 | F | 13 | H | 4 | W |
| 121.497 | 361 | U1474 | F | 13 | H | 4 | W |
| 121.997 | 361 | U1474 | F | 13 | H | 4 | W |
| 122.009 | 361 | U1474 | A | 13 | H | 2 | W |
| 124.789 | 361 | U1474 | A | 13 | H | 4 | W |
| 125.049 | 361 | U1474 | A | 13 | H | 4 | W |
| 127.879 | 361 | U1474 | A | 13 | H | 6 | W |
| 132.314 | 361 | U1474 | A | 14 | H | 2 | W |
| 135.114 | 361 | U1474 | A | 14 | H | 4 | W |
| 135.234 | 361 | U1474 | A | 14 | H | 4 | W |
| 138.354 | 361 | U1474 | A | 14 | H | 6 | W |
| 140.265 | 361 | U1474 | A | 15 | H | 2 | W |
| 143.025 | 361 | U1474 | A | 15 | H | 4 | W |
| 143.285 | 361 | U1474 | A | 15 | H | 4 | W |
| 146.345 | 361 | U1474 | A | 15 | H | 6 | W |
| 150.512 | 361 | U1474 | A | 16 | H | 2 | W |
| 151.872 | 361 | U1474 | A | 16 | H | 3 | W |
| 153.512 | 361 | U1474 | A | 16 | H | 4 | W |
| 156.492 | 361 | U1474 | A | 16 | H | 6 | W |
| 159.714 | 361 | U1474 | A | 17 | H | 2 | W |
| 162.604 | 361 | U1474 | A | 17 | H | 4 | W |
| 162.734 | 361 | U1474 | A | 17 | H | 4 | W |
| 165.744 | 361 | U1474 | A | 17 | H | 6 | W |
| 171.263 | 361 | U1474 | A | 18 | H | 2 | W |
| 173.873 | 361 | U1474 | A | 18 | H | 4 | W |
| 174.263 | 361 | U1474 | A | 18 | H | 4 | W |
| 177.273 | 361 | U1474 | A | 18 | H | 6 | W |
| 181.209 | 361 | U1474 | A | 19 | H | 2 | W |
| 184.049 | 361 | U1474 | A | 19 | H | 4 | W |
| 184.219 | 361 | U1474 | A | 19 | H | 4 | W |
| 187.249 | 361 | U1474 | A | 19 | H | 6 | W |

| | | | | | | | |
|---------|-----|-------|---|----|---|---|---|
| 193.015 | 361 | U1474 | A | 20 | H | 2 | W |
| 193.955 | 361 | U1474 | A | 20 | H | 3 | W |
| 196.025 | 361 | U1474 | A | 20 | H | 4 | W |
| 197.565 | 361 | U1474 | A | 20 | H | 5 | W |
| 205.957 | 361 | U1474 | A | 21 | H | 2 | W |
| 207.227 | 361 | U1474 | A | 21 | H | 3 | W |
| 208.947 | 361 | U1474 | A | 21 | H | 4 | W |
| 211.927 | 361 | U1474 | A | 21 | H | 6 | W |
| 216.915 | 361 | U1474 | A | 22 | H | 2 | W |
| 219.865 | 361 | U1474 | A | 22 | H | 4 | W |
| 220.115 | 361 | U1474 | A | 22 | H | 4 | W |
| 224.425 | 361 | U1474 | A | 23 | H | 2 | W |
| 227.275 | 361 | U1474 | A | 23 | H | 4 | W |
| 227.425 | 361 | U1474 | A | 23 | H | 4 | W |
| 230.415 | 361 | U1474 | A | 23 | H | 6 | W |
| 236.184 | 361 | U1474 | A | 24 | H | 2 | W |
| 237.374 | 361 | U1474 | A | 24 | H | 3 | W |
| 239.154 | 361 | U1474 | A | 24 | H | 4 | W |
| 244.048 | 361 | U1474 | A | 25 | H | 2 | W |
| 246.638 | 361 | U1474 | A | 25 | H | 4 | W |
| 247.058 | 361 | U1474 | A | 25 | H | 4 | W |
| 253.526 | 361 | U1474 | A | 26 | H | 2 | W |
| 255.916 | 361 | U1474 | A | 26 | H | 4 | W |
| 256.516 | 361 | U1474 | A | 26 | H | 4 | W |
| 258.886 | 361 | U1474 | A | 26 | H | 6 | W |
| 264.395 | 361 | U1474 | A | 27 | H | 3 | W |
| 265.565 | 361 | U1474 | A | 27 | H | 4 | W |
| 269.248 | 361 | U1474 | A | 28 | F | 2 | W |
| 275.578 | 361 | U1474 | A | 29 | F | 2 | W |
| 276.178 | 361 | U1474 | A | 29 | F | 2 | W |

Table 4, Table 5 and Table 6 in Supplement

Table 7:

| | Al2O3/CaO | Fe2O3/CaO | K2O/CaO | SiO2/CaO | TiO2/CaO |
|----------|------------|------------|------------|------------|------------|
| α | 0.80536554 | 0.82859485 | 1.25561443 | 0.64810943 | 0.65692594 |
| β | 4.73203445 | 0.86698091 | 0.87921402 | 3.57028639 | -1.3225902 |

Table captions

Table 1: List of discrete samples used for calibrating XRF concentrations

All samples listed are residues from the shipboard samples taken for MAD measurements from Hole A. Top Depth (m CCSF*) represents composite depths according to the "CCSF-361-U1474-ABDEF-20160220" depth scale and were specifically correlated visually using the magnetic susceptibility record of Hole A with that of the splice.

Table 2: Bulk sediment composition of U1474-A MAD residues

ICP-OES signal intensities were corrected for instrumental drift, corrected for blanks using the average of six total procedural blanks, then converted to concentrations using the accepted values for the following powdered rock standards: MAG-1, JA-1, GSP-2, SCO-1, JSI-1, and W-2 (Flanagan, 1984; Imai et al., 1996; McLennan & Taylor, 1980; Pretorius et al., 2006).

Table 3: CaCO₃% Measurements

Calcium carbonate measurements conducted via coulometry on the moisture and density sample residues, combined with CaCO₃% measurements taken aboard the *JOIDES Resolution*.

Table 7: XRF Calibration Model Parameters

Parameters α and β from Weltje and Tjallingii, 2008. These parameters are used in the equation $\alpha_i * [\text{XRF Ratio}_i] + \beta_i$, where i is the elemental ratio of interest.

Keywords

Include: Integrated Ocean Drilling Program, *JOIDES Resolution*, Expedition 361, South African Climates, Site U1474, XRF Core Scanning, Clay Mineralogy